

Decomposition of the Thermal Boundary Resistance across Carbon Nanotube–Graphene Junctions to Different Mechanisms

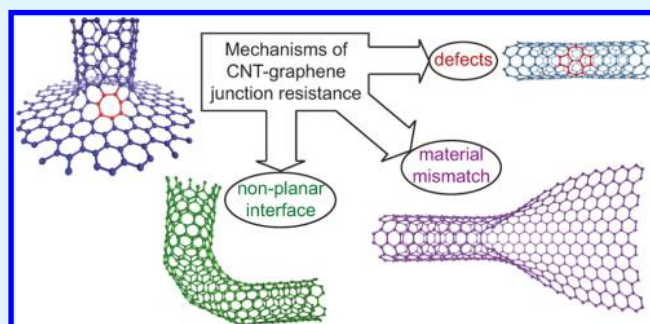
Jingjing Shi,[†] Yang Zhong,[†] Timothy S. Fisher,[‡] and Xiulin Ruan^{*,†}

[†]School of Mechanical Engineering and Birck Nanotechnology Center, Purdue University, West Lafayette, Indiana 47907, United States

[‡]Department of Mechanical and Aerospace Engineering & California NanoSystems Institute, University of California Los Angeles, Los Angeles, California 90095, United States

ABSTRACT: Three different mechanisms are identified to contribute to thermal resistances across a carbon nanotube–graphene junction: material mismatch, nonplanar junction, and defects. To isolate the contributions of each mechanism, we have designed five types of junctions and performed nonequilibrium molecular dynamics simulations. The results show that the contributions from the three mechanisms are similar, each at around $2.5 \times 10^{-11} \text{ m}^2 \text{ K/W}$. The relations between thermal boundary resistance and both defect number and turning angle at the interface are also studied.

KEYWORDS: carbon nanotubes, graphene, interface, thermal transport, molecular dynamics



1. INTRODUCTION

Materials with high thermal conductivity are needed to effectively dissipate heat from electronic devices. Although carbon nanotubes (CNTs)^{1–3} and graphene^{4–9} are promising high thermal conductivity materials, they both suffer from anisotropy in thermal transport.¹⁰ Hence, the idea of constructing three-dimensional interconnected structures with CNT, graphene, or both as building blocks has been proposed to achieve good thermal conductivity in all directions.^{11,12} These structures are also attractive for potential energy storage applications because of their large surface area,^{11,13–16} and it is timely to investigate their thermal properties. A pillared graphene system is one of these structures that has been synthesized recently.¹⁷ Previous nonequilibrium molecular dynamics (NEMD) simulations indicate that its thermal resistance primarily derives from CNT–graphene junctions.¹⁰ However, the NEMD method gives only an overall thermal boundary resistance (TBR) with few physical insights, and the thermal transport across an individual junction is not well-understood.

In this paper, we attempt to identify the different mechanisms and decompose the thermal resistance across a single CNT–graphene junction. We construct a series of structures to associate with each mechanism, and the NEMD method is used to calculate the TBRs. The relation between TBR and the number of defects at the interface is studied. The turning angle dependence of TBR is also explored.

2. METHODOLOGY

In earlier work,¹⁰ it is found that the resistance in pillared graphene mainly originates from the CNT–graphene junction,

and the diffusive limit of the junction resistance is about $7.5 \times 10^{-11} \text{ m}^2 \text{ K/W}$. This value is very low compared to other interfaces because of the strong sp^2 covalent bonding and absence of atomic mass mismatch. However, the junctions still introduce considerable overall resistance to the CNT–graphene network because of the extremely high thermal conductivity of CNTs and graphene. After inspecting the structure, we identified three possible mechanisms to investigate: materials mismatch, defects, and nonplanar interfaces.

Material mismatch involves phonons transport from one material (CNT) to a different material (graphene) as shown in Figure 1a, and the resistance comes from different phonon dispersion relations of CNT and graphene. Defects arise from six heptagons at the CNT–graphene junctions as shown in Figure 1b that introduce phonon-defect scattering. Nonplanar junctions require phonons to change the propagation direction by 90° as shown in Figure 1a, and the resistance comes from the change of phonon momentum. These mechanisms are coupled, and NEMD simulations can only give the overall resistance at the junction but not isolate different mechanisms. Hence, we have designed a series of related structures to decouple these mechanisms.

To isolate the defect mechanisms, the single-vacancy defect¹⁸ shown in Figure 2a and Stone–Wales defect¹⁹ shown in Figure 2b in a (6,6) CNT are considered where the nonplanar interface and material mismatch mechanisms are absent. To

Received: January 16, 2018

Accepted: April 3, 2018

Published: April 3, 2018

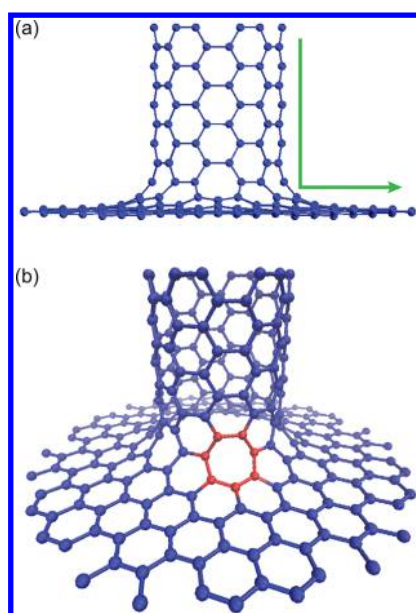


Figure 1. Orthogonal front view (a) and perspective view (b) of the detailed structure of a single CNT-graphene junction in pillared graphene. Red atoms form a heptagon.

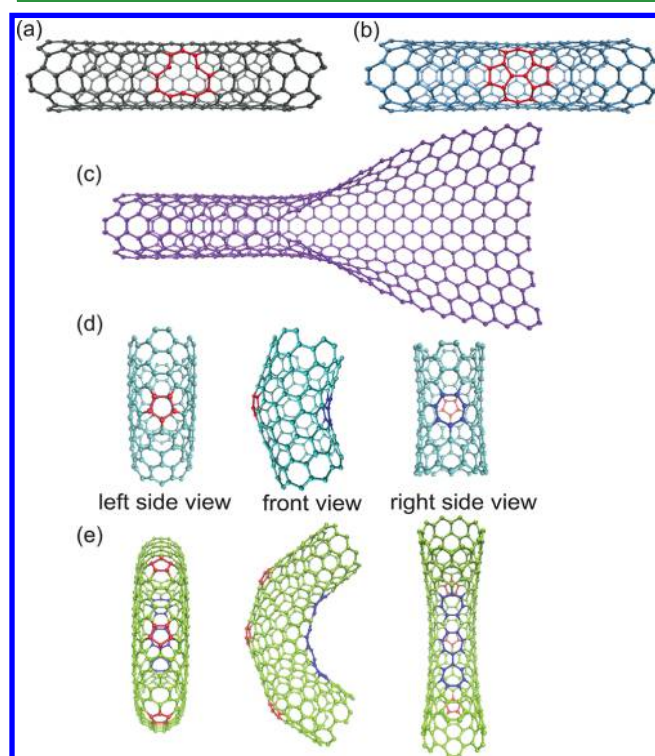


Figure 2. Interface structure of the single-vacancy defect (a), Stone-Wales defect (b), and unzipped (6,6) CNT (c); the left-side view, front view, and right-side view of 30° turning CNT (d) and 90° turning CNT (e).

isolate the material mismatch mechanism, the interface in an unzipped (6,6) CNT,²⁰ as shown in Figure 2c, is considered because it involves only material mismatch across the CNT and the graphene interface and does not involve any nonplanar junction or defect mechanisms. For the nonplanar interface mechanism, a 30° turning interface between a (6,6) CNT and a (10,0) CNT,²¹ as shown in Figure 2d, and a 90° turning

interface between a (6,6) CNT and a (10,0) CNT, as shown in Figure 2e, are considered. It should be noted that these turning CNTs also involve some degree of material mismatch (from chirality) and defects (pentagon and heptagon) because of the difficulty of identifying model CNT or graphene systems with the nonplanar interface mechanism only.

At the single-vacancy defect (Figure 2a), one carbon atom is missing. At the Stone-Wales defect (Figure 2b), one carbon-carbon bond turns vertically, and as a result, two pentagons and two heptagons are introduced into the pure (6,6) CNT previously with only hexagons. At the interface of an unzipped CNT (Figure 2c), the (6,6) CNT gradually transitions to a flat graphene nanoribbon. For the 30° turning CNT (Figure 2d), a pentagon gives a positive Gaussian curvature, while a heptagon gives a negative Gaussian curvature on the opposite side. The nonzero Gaussian curvature introduced by the heptagon and pentagon gives the cylindrical CNT a 30° turning. The interface of the 90° turning CNT (Figure 2e) is three 30° turning interfaces in series.

To obtain the interface thermal resistances of five different structures, NEMD simulations^{10,12,22} with the LAMMPS package are performed. The lengths of these structures along the heat transfer direction between two reservoirs are 100 nm, and the interface is at the center of the simulation domain. The lengths of the heat source and sink are both 10 nm. Interactions among carbon atoms are described by the AIREBO potential,²³ and the simulation time step is 0.4 fs. In a previous comparison study of different potentials,²⁴ it is found that the optimized Tersoff potential²⁵ is more accurate to describe phonon thermal properties of CNT and graphene. Here, we use the AIREBO potential because we want to compare to the previous results^{10,12} without any inconsistency of atomic potentials. In the simulation, a canonical NVT ensemble is run for 1.2 ns to relax the structure at first, allowing it to reach thermal equilibrium at 300 K. Then, it is switched to the microcanonical NVE ensemble. A constant heat flux is then added to the heat source and extracted from the heat sink for the next 8 ns. After the system reaches the steady state, the temperature of each small bin is obtained by averaging over 10 million time steps in the last 4 ns. The total number of temperature bins of (6,6) CNT from the reservoir to the interface is 406, and there is a half primitive cell (12 atoms) in each bin. For the graphene nanoribbon, the same number of temperature bins is used and there are 12 atoms in each bin because it is the unzipped (6,6) CNT. For the (10,0) CNT, the number of temperature bins from the reservoir to the interface is 234 and there is a half primitive cell of the (10,0) CNT (20 atoms) in each bin. Such temperature profiles are used to obtain thermal properties.

3. RESULTS AND DISCUSSION

3.1. Junction Resistance of Different Interfaces. Figure 3 shows the temperature profile of the 90° turning CNT in our simulation, and it is a typical temperature profile from NEMD. The temperature distributions in both the (6,6) and (10,0) CNTs are nearly linear, while at the interface an abrupt temperature jump exists. Hence, after linear fitting, the temperature jump ΔT_j at the junction can be calculated. The junction thermal boundary resistance R_j is given by

$$R_j = \frac{A_c \Delta T_j}{q} \quad (1)$$

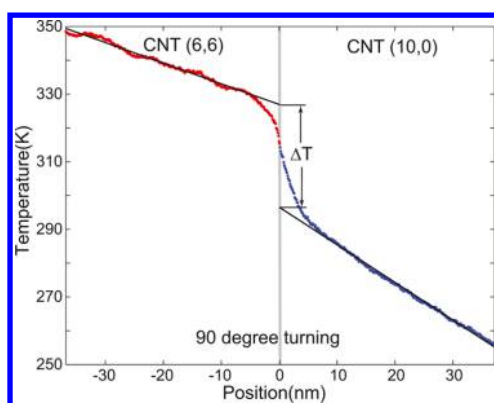


Figure 3. Temperature profile of 90° turning CNT in NEMD simulation.

Here, q is the heat flow rate and A_c is the cross-sectional area of a CNT. The value of A_c is $8.57 \times 10^{-19} \text{ m}^2$ for all five junctions, approximated as a circular ring of thickness 0.335 nm and radius 4.07 nm (average of inner and outer radius) which equals to the radius of the (6,6) CNT.

The thermal resistances of all the interfaces studied are shown in Table 1. The junction resistances of the single-

Table 1. Interface Thermal Resistance Results from NEMD of Different Interfaces

name	structure	defects	nonplanar	material mismatch	NEMD R_j ($\text{m}^2\text{K/W}$)
pillared graphene		X	X	X	7.5×10^{-11}
single-vacancy		X			2.3×10^{-11}
Stone-Wales		X			2.0×10^{-11}
unzipped CNT				X	2.8×10^{-11}
turning CNT		X	X	X	5.3×10^{-11}
vertically turning CNT		X	X	X	1.6×10^{-10}

vacancy and Stone–Wales are 2.3×10^{-11} and $1.9 \times 10^{-11} \text{ m}^2 \text{ K/W}$, respectively, which are approximately one-third of the resistance of the CNT–graphene junction. The resistance of a single vacancy is larger because one atom is missing, and three C–C bonds disappear because of the missing atom, while the number of C–C bonds does not change with the existence of the Stone–Wales defect. The heptagonal defect (Figure 1b) at the CNT–graphene junction is similar to the Stone–Wales defect because the number of C–C bonds does not decrease. The unzipped CNT junction shows a resistance of $2.8 \times 10^{-11} \text{ m}^2 \text{ K/W}$, which is also around one-third of the CNT–graphene junction resistance, again because of the fact that it only has one resistance mechanism (materials mismatch) out of the three. At the interface of unzipped CNT, only the material mismatch mechanism between (6,6) CNT and graphene exists. Hence, the resistance introduced by the material mismatch mechanism

is also about one-third of the pillared graphene interface. The resistance from the 30° turning CNT junction is about $5.3 \times 10^{-11} \text{ m}^2 \text{ K/W}$, which is larger than those from the single-vacancy defect, Stone–Wales defect, and unzipped CNT junction. This is probably because it involves not only the nonplanar interface mechanism but also defects (heptagon and pentagon) and material mismatch (from (6,6) CNT to (10,0) CNT). The resistance at the junction of the 90° turning CNT is about $1.6 \times 10^{-10} \text{ m}^2 \text{ K/W}$, which is three times that of the 30° turning junction. This result is reasonable because the 90° turning interface is just three 30° turning interfaces in series, and it shows that three 30° turning interfaces are not coupled. Our calculation indicates that all three mechanisms (defect, material mismatch, and nonplanar interface) contribute nearly equally to the CNT–graphene junction resistance.

3.2. Error Analysis. There are statistical and systematic errors in the NEMD simulations.²⁶ The statistical error of TBR from NEMD simulations is usually considered small. To verify that our results are reliable, six separate NEMD simulations were conducted on the same (6,6) CNT with the Stone–Wales defect structure with different initial atom velocities in the MD simulations generated from different seeds. The results of the TBR at the interface of a Stone–Wales defect from six trials are shown in Figure 4a. The results from different trials are very similar to each other and close to the average. The standard deviation for this sample of six independent simulations is only 5.4% of the average resistance, and the uncertainty should be small.

The most important systematic error in NEMD simulations of TBR comes from the finite-size effect.^{10,22,27,28} The domain-size dependence of TBR in NEMD simulations is because that the largest phonon wavelength is directly determined by the domain size, and long mean free path phonon can ballistically transport through if the mean free path is larger than or comparable to the domain size. Hence, to find the diffusive limit, a domain size which is large enough is needed. The relation between the domain size and the TBR at the Stone–Wales defect is studied to find the proper simulation domain length. The results of boundary resistance with different domain sizes are shown in Figure 4b. From the results, it can be seen that when L , the CNT length between two reservoirs, is larger than 80 nm, the resistance nearly does not change with the increase of L . In our simulation, L is 100 nm, and it should be reasonable to assume that the results from our NEMD simulations reach the diffusive limit.

3.3. Relation between Resistance and the Number of Defects. The relation between the junction thermal resistance and the number of defects is studied here because there are six heptagon defects at the CNT–graphene junction. The defects can be either in series (defects are distributed along the CNT axial direction) or in parallel (defects are distributed evenly along the CNT tangential direction) as shown in Figure 5, and both cases with single-vacancy or Stone–Wales defect have been explored.

As shown clearly in Table 2, the relation between the total resistance of defects in series and the number of defects follows a similar trend for both single-vacancy and Stone–Wales defects. The total resistance values of two and three single-vacancy defects in series are 1.4 and 2.2 times the resistance of one single-vacancy defect respectively, while the total resistance values of two and three Stone–Wales defects in series are 1.3 and 2.1 times the resistance of one Stone–Wales defect, respectively. It indicates that these defects in series are coupled

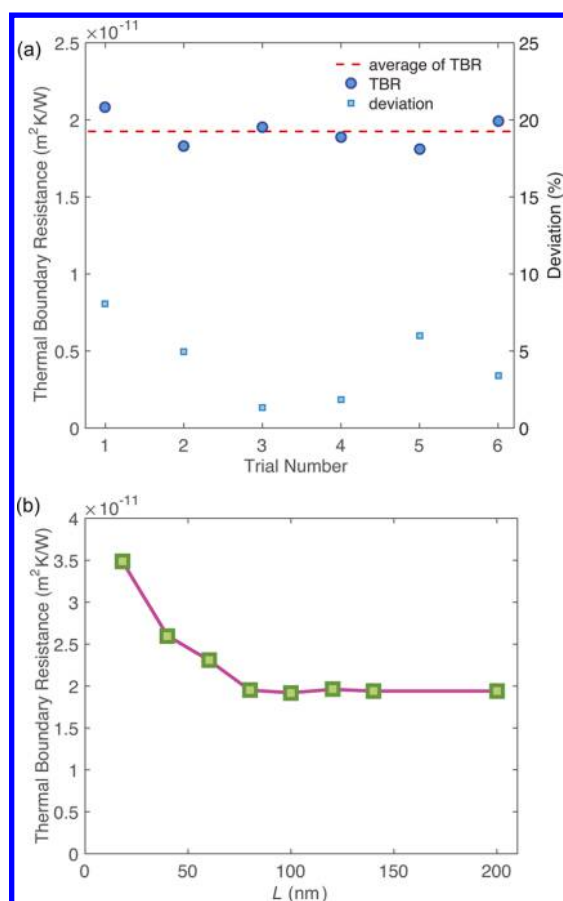


Figure 4. (a) TBR results and the corresponding deviation percentage from the average at a Stone–Wales defect in (6,6) CNT with different initial velocities from NEMD simulations (the left axis is the scale of TBR, the right axis is the scale of deviation percentage). The red dashed line is the average TBR of the six trials. (b) TBR results at a Stone–Wales defect in (6,6) CNT with different domain sizes in NEMD simulations. L is the length of CNT along the heat transfer direction between reservoirs.

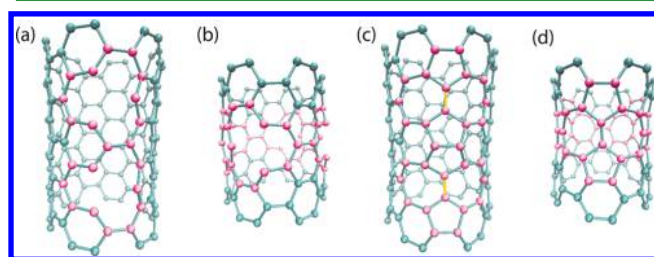


Figure 5. (a) Two single-vacancy defects in series, (b) four single-vacancy defects in parallel, (c) two Stone–Wales defects in series, and (d) three Stone–Wales defects in parallel. Pink atoms are directly affected by defects.

when they are very close to each other, and as a result, the total resistance is smaller than the number of defects times the resistance of a single defect.

For the defects in parallel, the total resistance of two and three single-vacancy defects in parallel are 1.7 and 3.2 times the resistance of one single-vacancy defect respectively, and the resistance of two and three Stone–Wales defects in parallel are 1.9 and 3.9 times the resistance of one Stone–Wales defect, respectively. Unlike the defects in series, the total resistance of defects in parallel can be larger than the resistance of a single

Table 2. NEMD Interface Thermal Resistance Results of Different Number of Defects

defect type	number of defects	in series	in parallel	NEMD R_i ($\text{m}^2 \text{K/W}$)
single-vacancy	2	×		3.4×10^{-11}
	3	×		5.2×10^{-11}
	2		×	3.9×10^{-11}
	3		×	7.5×10^{-11}
	4		×	1.0×10^{-10}
	6		×	1.7×10^{-10}
Stone–Wales	2	×		2.6×10^{-11}
	3	×		4.2×10^{-11}
	2		×	3.7×10^{-11}
	3		×	7.8×10^{-11}
			×	

defect times the number of defects. Moreover, as mentioned earlier that the resistance of one single-vacancy defect is larger than the resistance of one Stone–Wales defect because of the reduced number of C–C bonds. However, the total resistance of more than two single-vacancy defects is smaller than the corresponding resistance of Stone–Wales defects. These phenomena can be explained by that, as shown in Figure 2a,b, there are 12 columns of hexagons in the axial direction of (6,6) CNT, and for one single-vacancy defect, two columns will be directly affected, while for one Stone–Wales defect, three columns will be directly affected. The total resistance of four and six single-vacancy defects in parallel are 4.5 and 7.3 times the resistance of one single-vacancy defect, respectively. If we consider the hexagon columns not directly affected, for four single-vacancy defects in parallel, only four columns (one-third of the total) are not directly affected, while for six single-vacancy defects in parallel, all the columns are affected. Hence, with the existence of defects in parallel, the total resistance might be higher than the defect number times the resistance of a single defect. Also, because one more hexagon column will be affected by the Stone–Wales defect than by single-vacancy, with the increase of defect number, the hexagon columns not directly affected by Stone–Wales defects will be much less than those by single-vacancy defect for the same number of defects. Therefore, it is reasonable that the total resistance of Stone–Wales defect exceeds that of single-vacancy defect when the defect number is large. At the CNT–graphene junction, each of the six heptagon defects in parallel only affects one column of C–C bonds, and as a result, the resistance from defects is relatively small compared to single-vacancy and Stone–Wales defects. Considering that there are six columns of hexagons affected at the CNT–graphene interface, the resistance from defects at the interface should be comparable to but smaller than that of two Stone–Wales defects in parallel (because three columns of hexagons are affected for each Stone–Wales defect), which is 3.7×10^{-11} $\text{m}^2 \text{K/W}$. Hence, the estimated value for the CNT–graphene junction thermal resistance from defects is about 3×10^{-11} $\text{m}^2 \text{K/W}$, which is about one-third of the total resistance at the CNT–graphene junction.

3.4. Relation between Resistance and the Turning Angle. Now, we explore further on how an abrupt versus gradual turning angle affects interface thermal resistance across the CNT–graphene junction by a CNT–nanocone–graphene structure. By changing the apex angle of the carbon nanocone between the CNT and graphene, we can tune the phonon transport path as shown in Figure 6. The NEMD method with the same simulation time step and number of steps has been

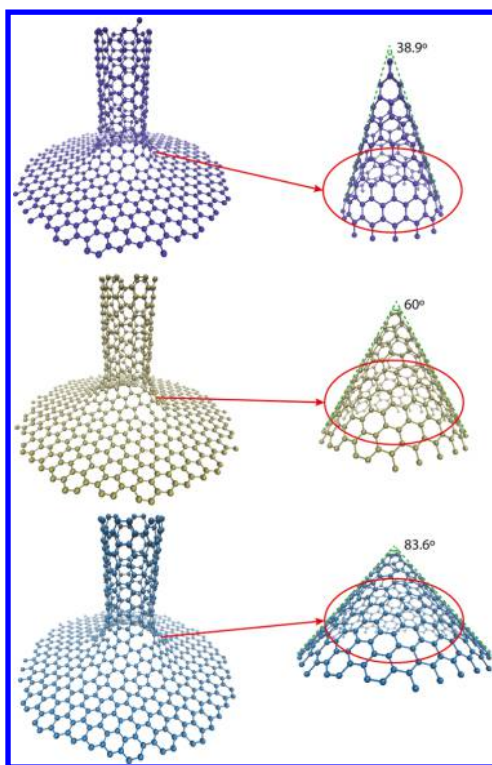


Figure 6. CNT–nanocone–graphene structures with different carbon nanocone apex angles.

used in our calculation. The length of the (6,6) CNT is 50 nm, the height of the nanocone between CNT and graphene sheet is 0.6 nm, and the graphene is 31×31 nm. The resistances of 38.9° , 60° , and 83.6° apex angle nanocone interface are 1.9×10 , 1.8×10^{-10} , and 1.9×10^{-10} m² K/W, respectively. There is not much difference from different CNT–nanocone–graphene structures, probably because there are a lot of defects at the interface, rendering the main mechanism leading to resistance to be defects. As a result, the resistance is not sensitive to different nanocone apex angles.

4. CONCLUSIONS

To summarize, we have identified three mechanisms which can lead to thermal resistances across the pillared graphene junction: the material mismatch, the nonplanar junction, and defects. NEMD simulations have been performed to compare five types of different junctions (unzipped CNT, CNT with single-vacancy, CNT with Stone–Wales defects, 30° CNT–CNT junction, and 90° CNT–CNT junction) corresponding to different mechanisms. The corresponding junction thermal resistance results from NEMD show that the junction resistances from different mechanisms are on the same order of magnitude. Both defect number and turning angle dependence of TBR have been explored. The results show that the defects in series are coupled and the total resistance is smaller than the defect number times the resistance of a single defect. For the defects in parallel, the total resistance is related to the number of CNT hexagon columns affected by the defects. If the defects are very dense, the resistance can be higher than the defect number times the resistance of a single defect. These findings can be used to estimate the resistance at the interface of carbon-based hierarchical structures.

AUTHOR INFORMATION

Corresponding Author

*E-mail: ruan@purdue.edu.

ORCID

Jingjing Shi: 0000-0002-0249-4468

Timothy S. Fisher: 0000-0002-8909-313X

Xiulin Ruan: 0000-0001-7611-7449

Notes

The authors declare no competing financial interest.

ACKNOWLEDGMENTS

The authors acknowledge the support by the Air Force Office of Scientific Research (AFOSR) MURI grant (FA9550-12-1-0037).

REFERENCES

- (1) Lindsay, L.; Broido, D. A.; Mingo, N. Diameter dependence of carbon nanotube thermal conductivity and extension to the graphene limit. *Phys. Rev. B: Condens. Matter Mater. Phys.* **2010**, *82*, 161402.
- (2) Shiomi, J.; Maruyama, S. Non-Fourier heat conduction in a single-walled carbon nanotube: Classical molecular dynamics simulations. *Phys. Rev. B: Condens. Matter Mater. Phys.* **2006**, *73*, 205420.
- (3) Qiu, B.; Wang, Y.; Zhao, Q.; Ruan, X. The effects of diameter and chirality on the thermal transport in free-standing and supported carbon-nanotubes. *Appl. Phys. Lett.* **2012**, *100*, 233105.
- (4) Balandin, A. A.; Ghosh, S.; Bao, W.; Calizo, L.; Teweldebrhan, D.; Miao, F.; Lau, C. N. Superior Thermal Conductivity of Single-Layer Graphene. *Nano Lett.* **2008**, *8*, 902–907.
- (5) Ghosh, S.; Calizo, I.; Teweldebrhan, D.; Pokatilov, E. P.; Nika, D. L.; Balandin, A. A.; Bao, W.; Miao, F.; Lau, C. N. Extremely high thermal conductivity of graphene: Prospects for thermal management applications in nanoelectronic circuits. *Appl. Phys. Lett.* **2008**, *92*, 151911–151913.
- (6) Lindsay, L.; Broido, D. A.; Mingo, N. Flexural phonons and thermal transport in graphene. *Phys. Rev. B: Condens. Matter Mater. Phys.* **2010**, *82*, 115427.
- (7) Hu, J.; Ruan, X.; Chen, Y. P. Thermal Conductivity and Thermal Rectification in Graphene Nanoribbons: A Molecular Dynamics Study. *Nano Lett.* **2009**, *9*, 2730–2735.
- (8) Wang, Y.; Qiu, B.; Ruan, X. Edge effect on thermal transport in graphene nanoribbons: A phonon localization mechanism beyond edge roughness scattering. *Appl. Phys. Lett.* **2012**, *101*, 013101.
- (9) Qiu, B.; Ruan, X. Reduction of spectral phonon relaxation times from suspended to supported graphene. *Appl. Phys. Lett.* **2012**, *100*, 193101.
- (10) Shi, J.; Dong, Y.; Fisher, T.; Ruan, X. Thermal transport across carbon nanotube-graphene covalent and van der Waals junctions. *J. Appl. Phys.* **2015**, *118*, 044302.
- (11) Dimitrakakis, G. K.; Tyliaakis, E.; Froudakis, G. E. Pillared Graphene: A New 3-D Network Nanostructure for Enhanced Hydrogen Storage. *Nano Lett.* **2008**, *8*, 3166–3170.
- (12) Varshney, V.; Patnaik, S. S.; Roy, A. K.; Froudakis, G.; Farmer, B. L. Modeling of Thermal Transport in Pillared-Graphene Architectures. *ACS Nano* **2010**, *4*, 1153–1161.
- (13) Che, G.; Lakshmi, B. B.; Fisher, E. R.; Martin, C. R. Carbon nanotubule membranes for electrochemical energy storage and production. *Nature* **1998**, *393*, 346–349.
- (14) Vix-Guterl, C.; Frackowiak, E.; Jurewicz, K.; Friebe, M.; Parmentier, J.; Béguin, F. Electrochemical energy storage in ordered porous carbon materials. *Carbon* **2005**, *43*, 1293–1302.
- (15) Wang, D.-W.; Li, F.; Liu, M.; Lu, G. Q.; Cheng, H.-M. 3D Aperiodic Hierarchical Porous Graphitic Carbon Material for High-Rate Electrochemical Capacitive Energy Storage. *Angew. Chem., Int. Ed.* **2008**, *47*, 373–376.
- (16) Aboutalebi, S. H.; Jalili, R.; Esrafilzadeh, D.; Salari, M.; Gholamvand, Z.; Yamini, S. A.; Konstantinov, K.; Shepherd, R. L.;

Chen, J.; Moulton, S. E.; Innis, P. C.; Minett, A. I.; Razal, J. M.; Wallace, G. G. High-Performance Multifunctional Graphene Yarns: Toward Wearable All-Carbon Energy Storage Textiles. *ACS Nano* **2014**, *8*, 2456–2466.

(17) Xue, Y.; Ding, Y.; Niu, J.; Xia, Z.; Roy, A.; Chen, H.; Qu, J.; Wang, Z. L.; Dai, L. Rationally designed graphene-nanotube 3D architectures with a seamless nodal junction for efficient energy conversion and storage. *Sci. Adv.* **2015**, *1*, No. e1400198.

(18) Mielke, S. L.; Troya, D.; Zhang, S.; Li, J.-L.; Xiao, S.; Car, R.; Ruoff, R. S.; Schatz, G. C.; Belytschko, T. The role of vacancy defects and holes in the fracture of carbon nanotubes. *Chem. Phys. Lett.* **2004**, *390*, 413–420.

(19) Chandra, N.; Namilae, S.; Shet, C. Local elastic properties of carbon nanotubes in the presence of Stone-Wales defects. *Phys. Rev. B: Condens. Matter Mater. Phys.* **2004**, *69*, 094101.

(20) Kosynkin, D. V.; Higginbotham, A. L.; Sinitiskii, A.; Lomeda, J. R.; Dimiev, A.; Price, B. K.; Tour, J. M. Longitudinal unzipping of carbon nanotubes to form graphene nanoribbons. *Nature* **2009**, *458*, 872–876.

(21) Yao, Z.; Postma, H. W. C.; Balents, L.; Dekker, C. Carbon nanotube intramolecular junctions. *Nature* **1999**, *402*, 273–276.

(22) Schelling, P. K.; Phillpot, S. R.; Keblinski, P. Comparison of atomic-level simulation methods for computing thermal conductivity. *Phys. Rev. B: Condens. Matter Mater. Phys.* **2002**, *65*, 144306.

(23) Brenner, D. W.; Shenderova, O. a.; Harrison, J. a.; Stuart, S. J.; Ni, B.; Sinnott, S. B. A second-generation reactive empirical bond order (REBO) potential energy expression for hydrocarbons. *J. Phys.: Condens. Matter* **2002**, *14*, 783–802.

(24) Zou, J.-h.; Ye, Z.-q.; Cao, B.-y. Phonon thermal properties of graphene from molecular dynamics using different potentials. *J. Chem. Phys.* **2016**, *145*, 134705.

(25) Lindsay, L.; Broido, D. A. Optimized Tersoff and Brenner empirical potential parameters for lattice dynamics and phonon thermal transport in carbon nanotubes and graphene. *Phys. Rev. B: Condens. Matter Mater. Phys.* **2010**, *81*, 205441.

(26) Stevens, R. J.; Zhigilei, L. V.; Norris, P. M. Effects of temperature and disorder on thermal boundary conductance at solid-solid interfaces: Nonequilibrium molecular dynamics simulations. *Int. J. Heat Mass Transfer* **2007**, *50*, 3977–3989.

(27) Salaway, R. N.; Zhigilei, L. V. Molecular dynamics simulations of thermal conductivity of carbon nanotubes: Resolving the effects of computational parameters. *Int. J. Heat Mass Transfer* **2014**, *70*, 954–964.

(28) Liang, Z.; Keblinski, P. Finite-size effects on molecular dynamics interfacial thermal-resistance predictions. *Phys. Rev. B: Condens. Matter Mater. Phys.* **2014**, *90*, 075411.